nature photonics

Article

https://doi.org/10.1038/s41566-022-01115-7

Geometric filterless photodetectors for mid-infrared spin light

Received: 6 March 2022

Accepted: 20 October 2022

Published online: 5 December 2022

Check for updates

Jingxuan Wei[1], Yang Chen[2], Ying Li[3,4], Wei Li[5], Junsheng Xie[1,6], Chengkuo Lee[1,6] ✉, Kostya S. Novoselov[7] & Cheng-Wei Qiu[1] ✉

Free-space circularly polarized light (CPL) detection, requiring polarizers and wave plates, is well established, but such a spatial degree of freedom is unfortunately absent in integrated on-chip optoelectronics. The filterless CPL photodetectors reported so far suffer from an intrinsic small discrimination ratio, vulnerability to the non-CPL field components and low responsivity. Here we report a distinct paradigm of geometric photodetectors in the mid-infrared, exhibiting a substantial discrimination ratio of 84, a close-to-perfect CPL-specific response, a zero-bias responsivity of 392 V W^{-1} at room temperature and a detectivity of ellipticity down to 0.03° $Hz^{-1/2}$. Our approach makes use of a plasmonic nanostructures array with judiciously designed symmetry, assisted by graphene ribbons, to electrically read their near-field optical information. This geometry-empowered recipe for infrared photodetectors provides a robust, direct, strict and high-quality solution to on-chip filterless CPL detection and unlocks new opportunities for integrated functional optoelectronic devices.

Polarization, a dimension of light beyond intensity and wavelength, plays a pivotal and ubiquitous role in a number of optical technologies[1–3]. Circularly polarized light (CPL), also known as spin light, which carries spin angular momentum, enables widespread applications such as drug screening[4], quantum optics[5], imaging[6] and biosensing[7]. Conventionally, the detection of CPL requires a set of bulky polarization optics, because commercial photodetectors are only sensitive to the light intensity, imposing difficulties for miniaturized systems. One possible solution is flat optics, where the filters and wave plates can be replaced by ultrathin metasurfaces[8–10]. However, this arrangement still relies on a propagation distance in space between the metasurfaces and detectors[1,11,12], multiple measurements to disentangle the different polarization states, accurate alignment and heterogeneous integration[13,14], preventing the implementation of cost-effective monolithic systems. This has led to the development of novel photodetectors natively sensitive to the spin state of light[15–17]. So far, to the best of our knowledge, there are three main approaches to designing spin-sensitive photodetectors. In the first, chiral molecules with circular dichroism can be used in a phototransistor configuration for high-responsivity CPL detection[15,17–19]. However, the discrimination ratio of the photoresponse to left-handed and right-handed CPL (LCP and RCP), $g_{ph} = |(I_{LCP} - I_{RCP})/(I_{LCP} + I_{RCP})|$, is intrinsically small because of the weak chiroptic response in molecules. Furthermore, these devices are usually vulnerable to unpolarized and linearly polarized light. Second, artificial plasmonic structures can provide larger circular dichroism, but an efficient way of transferring the chiroptical response to an electrical signal readout remains lacking[16,20–22]. Third, a CPL-sensitive photoresponse also exists in the circular photogalvanic effect[23,24], the photon drag effect[25,26] and

[1]Department of Electrical and Computer Engineering, National University of Singapore, Singapore, Singapore. [2]CAS Key Laboratory of Mechanical Behaviour and Design of Materials, Department of Precision Machinery and Precision Instrumentation, University of Science and Technology of China, Hefei, China. [3]Interdisciplinary Center for Quantum Information, State Key Laboratory of Modern Optical Instrumentation, ZJU-Hangzhou Global Scientific and Technological Innovation Center, Zhejiang University, Hangzhou, China. [4]International Joint Innovation Center, Key Lab of Advanced Micro/Nano Electronic Devices & Smart Systems of Zhejiang, Zhejiang University, Haining, China. [5]GPL Photonics Lab, State Key Laboratory of Applied Optics, Changchun Institute of Optics, Fine Mechanics and Physics, Chinese Academy of Sciences, Changchun, China. [6]Center for Intelligent Sensors and MEMS, National University of Singapore, Singapore, Singapore. [7]Institute for Functional Intelligent Materials, National University of Singapore, Singapore, Singapore. ✉e-mail: elelc@nus.edu.sg; chengwei.qiu@nus.edu.sg

the spin-galvanic effect[27], but the responsivities of these are still too low for most practical applications.

Practically speaking, an effective monolithic CPL detector needs to meet the following three criteria: (1) it should be possible for left- and right-handed CPL to be well discriminated[15,24]; (2) the detection of CPL should be robust, with immunity against the ubiquitous unpolarized and linearly polarized light[22,28]; and (3) the responsivity and signal-to-noise ratio should be sufficiently large for practical applications[6]. These criteria can also be mathematically formulated. We first write the general expression for a polarization-dependent photoresponse: $V_{ph} = R_0 \times S_0 + R_1 \times S_1 + R_2 \times S_2 + R_3 \times S_3$, where $R_{0,1,2,3}$ are the respective responsivities to the four Stokes parameters, $S_{0,1,2,3}$ (Supplementary Note 1 provides a detailed discussion). Note that S_0, S_1, S_2 and S_3 represent the intensity of light, two linearly polarized components and the circularly polarized light component, respectively[6]. A perfect CPL photodetector should follow

$$V_{ph} = R_3 \times S_3, \quad (1)$$

meaning that R_3 dominates in the photoresponse over $R_{0,1,2}$. Notably, the above equation also indicates that LCP ($S_3 = -1$) and RCP ($S_3 = 1$) light will lead to an opposite photoresponse, so they can be markedly discriminated by the photovoltage sign, regardless of their intensities. The concept of such an ideal CPL-specific detector can be better visualized by the Poincaré sphere, as shown in Fig. 1a. However, it remains elusive to realize such rigid CPL photodetectors with high performance.

In this article, we showcase how the symmetry and geometry of a plasmonic-nanostructures array, in combination with patterned graphene ribbons, come into a synergetic play to enable the on-chip specific detection of CPL with an unusually large discrimination ratio, immunity to non-CPL field components and high responsivity. Our contributions are threefold. First, we reveal that the vectorial photoresponse generated from achiral structures could reach a symmetry-protected infinite discrimination ratio, g_{ph}, superior to existing works based on circular dichroism where g_{ph} is naturally constrained below one[15–17]. Second, we demonstrate how the geometric arrangement of plasmonic nanostructures can power up the specific detection of CPL. Third, we report how the patterned graphene sheet enhances the efficiency in reading the near-field information of the plasmonic nanostructures. Our graphene-ribbon device achieves a peak responsivity of 392 V W^{-1} for the individual nanostructures and a detectivity of ellipticity down to 0.03° Hz$^{-1/2}$ in the mid-infrared at room temperature.

Results

Methodology

Figure 1b presents a scanning electron microscopy (SEM) image of one design of our CPL-specific photodetector. This two-port device features a ring-shaped few-layer graphene device channel and a circularly arranged metallic T-shaped array of nanoantennas (see Supplementary Fig. 4 for the thickness measurements). Devices with other geometries (such as half rings and rectangles) will be discussed later.

The methodology of our experiment is outlined in Fig. 1c. The responsivities of the photodetectors to the four Stokes parameters were studied by modulating the incident beam with a quarter-wave plate (QWP). The incident light is purely coherent and is linearly polarized along the x axis, so the polarization state of light after passing the QWP can be described with a new set of Stokes parameters (Supplementary Note 2 presents the derivation)—$S_0 = 1$; $S_1 = 0.5 + 0.5\cos(4\varphi)$; $S_2 = 0.5\sin(4\varphi)$; $S_3 = \sin(2\varphi)$—where φ is the angle of the fast axis of the QWP (Fig. 1d). Because the four Stokes parameters show non-synchronous dependence on the QWP angle, their respective contributions to the photoresponse in our device can be extracted. The incident light is at a wavelength of 4 μm and normal to the device. In our experiments, we always use open-circuit voltages as the photoresponse unless otherwise stated. Figure 1e shows the measured φ-dependent photoresponse, which nicely follows a $\sin(2\varphi)$ function. From the general expression for the QWP angle-dependent photovoltage, $V_{ph} \propto R_0 + R_1 \times (0.5 + 0.5\cos(4\varphi)) + R_2 \times 0.5\sin(4\varphi) + R_3 \times \sin(2\varphi)$, we can extract the respective normalized responsivities, $R_{0,1,2,3} \approx (-0.013, -0.006, -0.072, 1)$, confirming that R_3 is ten times larger than the sum of R_0, R_1 and R_2. Notably, the discrimination ratio, $g_{ph} = |R_3/R_0| = 84$, even breaks the limit of one in conventional CPL detectors based on circular dichroism[15–17]. We can thus conclude that our device meets the first two criteria of an ideal CPL-specific photodetector. The measured R_3 at room temperature reaches 1.8 V W^{-1} (see Supplementary Fig. 5 for an estimation of the incident power). Much larger responsivities can also be achieved, as discussed later.

Mirror-symmetric meta-atoms

The design principle of our proposed plasmonic nanostructures is illustrated in Fig. 2a. Because CPL possesses handedness, it is commonly deemed that CPL-sensitive photodetectors need to break mirror symmetry in geometry[29–31]. However, this perception can be challenged by closer scrutiny of the symmetry analysis. Although the mirror symmetry in achiral structures prohibits a different absorption between LCP and RCP illumination, a CPL-sensitive vectorial photoresponse could exist, for example, the photocurrent along x-axis, J_x, which is parity-odd to the reflection operation. More interestingly, achiral symmetry forces J_x under LCP and RCP illumination to be equal in magnitude but with opposite sign, so the photoresponse discrimination ratio, $g_{ph} = |(J_{x,LCP} - J_{x,RCP})/(J_{x,LCP} + J_{x,RCP})|$, will approach infinity, in sharp contrast to the case in absorption-based chiral devices, where g_{ph} is constrained to be below one[15–17]. Further analysis reveals that the symmetry-protected infinite g_{ph} should only be available when the nanostructures contain a single mirror symmetry axis (Supplementary Note 3).

With a view to implementing the vectorial photoresponse with infinite g_{ph}, we study the near-field of nanophotonic structures. Recent works, via cathodoluminescence microscopy, have revealed a giant chirality 'hidden' in the near-field profile of mirror-symmetric achiral nanostructures, which originates from the interference of multiple modes[32–35]. However, efficient reading of the near-field chirality with an electrical output remains elusive and unexplored. Following previous works[36,37], we propose achieving the realization of this transfer process by placing a graphene sheet below the plasmonic nanostructures. Due to Fermi-level misalignment, the graphene covered by the metals becomes doped[38], so its Seebeck coefficient is also tuned[39], forming a Seebeck gradient at the graphene–metal interfaces. When these interfaces are illuminated by an enhanced light field, hot electrons are generated and driven by the Seebeck gradient, forming nonlocal directional photocurrents[40,41] (experimental validation of this is provided in Supplementary Fig. 6). We note that intrinsic graphene plasmons should not play an essential role in our device, because they cannot be excited efficiently at this wavelength (Supplementary Fig. 7). Besides, the hot electrons in metallic nanostructures arising due to the decay of surface plasmons cannot account for the measured photoresponse, given their low photon-to-electron conversion efficiency[16]. Note that the near-field chirality of plasmonic nanostructures should not be confused with the super-chiral field (Supplementary Fig. 26). Detailed theoretical analysis of the near-field asymmetry and the resulting CPL-sensitive photoresponse is provided in Supplementary Note 4.

We further optimize the geometric parameters of the plasmonic nanostructures by numerically calculating the CPL-sensitive J_x (simulation details are provided in Supplementary Fig. 8). Figure 2b shows the results at different horizontal lengths h and vertical lengths v of the nanostructures under RCP illumination. The width w and thickness of the nanostructures were kept at 0.1 μm and 0.06 μm, respectively. The optimized dimensions of the nanostructure are $h = 1.1$ μm and $v = 0.75$ μm. Supplementary Fig. 9 presents an experimental validation of our calculations.

https://doi.org/10.1038/s41566-022-01115-7

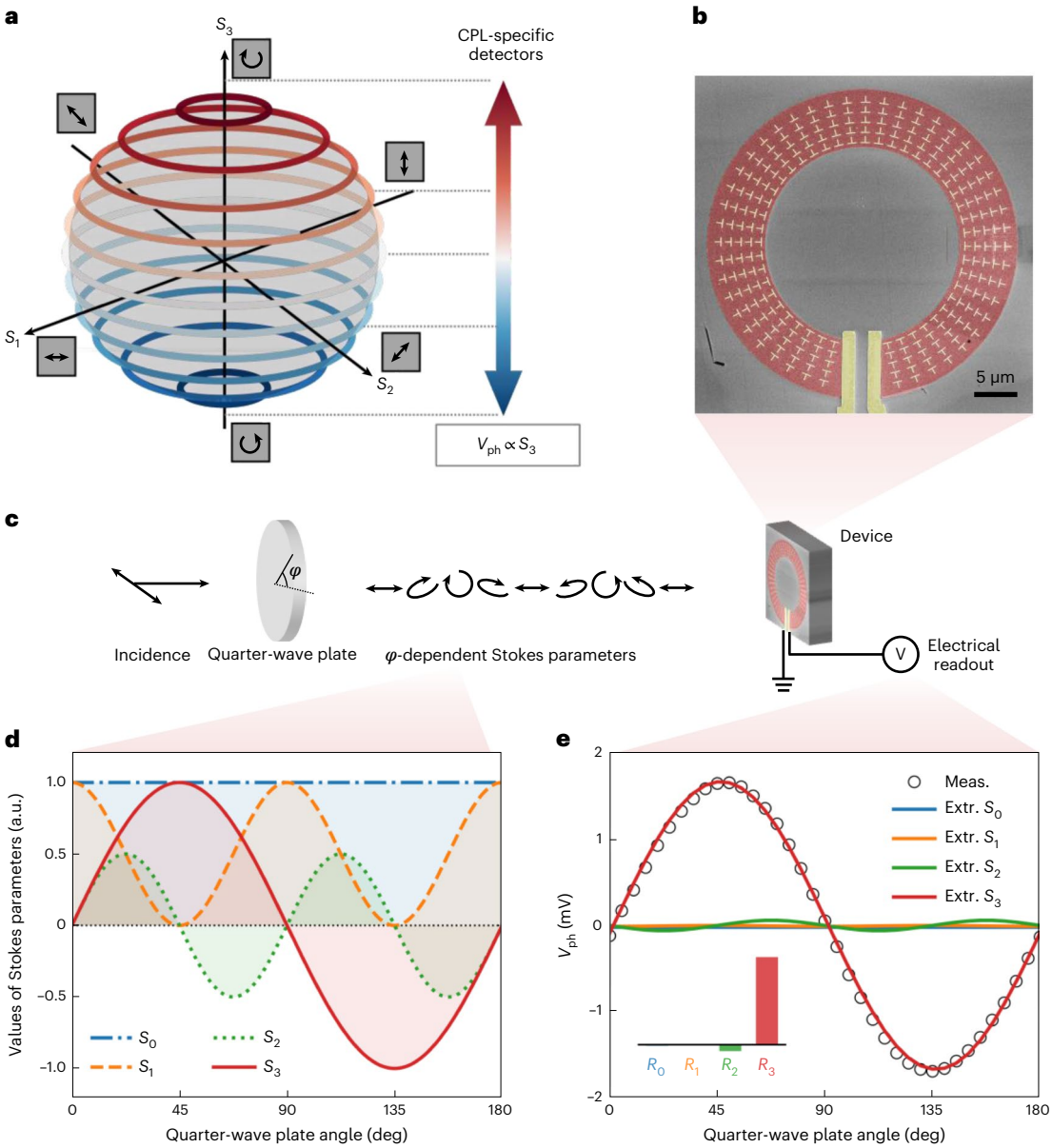

Fig. 1 | Concept of geometric photodetectors for CPL-specific detection. a, Illustration of CPL-specific photodetectors in the Poincaré sphere, where the photoresponse, V_{ph}, only depends on the fourth Stokes parameter of the incident light, S_3. **b**, False-coloured SEM image of our ring-shaped device, consisting of geometrically arranged mirror-symmetric plasmonic nanostructures on a graphene sheet. Colour code: graphene, red; plasmonic nanostructures and electrodes, yellow; substrate, grey. **c**, Schematic of the experimental set-up and methodology. The responsivities of our device to the four Stokes parameters are studied by rotating a QWP and then reading the electrical output of our device. **d**, Calculated dependence of Stokes parameters on the QWP angle. **e**, Experimentally measured QWP angle-dependent photovoltages and the extracted contributions from $S_{0,1,2,3}$, under a normally incident illumination at 4-μm wavelength. Inset: the extracted responsivities, $R_{0,1,2,3}$, confirming the dominance of CPL sensitivity in our device. The incident power is 0.9 mW.

We then take a closer look at the optimal geometry. As expected, the achiral nanoantenna identically absorbs the LCP and RCP light, showing no circular dichroism (Fig. 2c). Notably, there is a wavelength shift in the absorption peaks under the *x*-axis and *y*-axis linearly polarized illumination; this is usually a feature of the chirality-dependent mode interference and hence the near-field chirality (Supplementary Note 4). Based on the simulation shown in Fig. 2d,e, the near-field profile is indeed highly asymmetric, with an intensity ratio of 6 (see the cutline plot in Supplementary Fig. 10), and flips horizontally when the handedness of the CPL changes, leading to opposite average J_x and identical average J_y (experimental validation is provided in Supplementary Fig. 11). To better illustrate our design principle, we plot the absorption spectra and near-field of the plasmonic nanostructure (h = 1.1 μm and v = 0.6 μm) with an almost vanishing CPL response. In this case, there is no pronounced wavelength shift in the absorption peaks (Fig. 2f), indicating a weak near-field chirality. The resulting near-field distribution is almost symmetric along the *y* axis, leading to a very small CPL-sensitive photoresponse, J_x (Fig. 2g,h). We have thus theoretically realized symmetry-protected infinite g_{ph} in achiral structures with no circular dichroism, fulfilling the first criterion of ideal CPL detectors.

Geometrically arranged meta-atoms

The second criterion requires our device to be specific to CPL, namely, immune against both unpolarized and linearly polarized light. By analyzing the simulated polarization dependence of J_x (Supplementary Fig. 12), we can extract the respective normalized responsivities to the four

https://doi.org/10.1038/s41566-022-01115-7

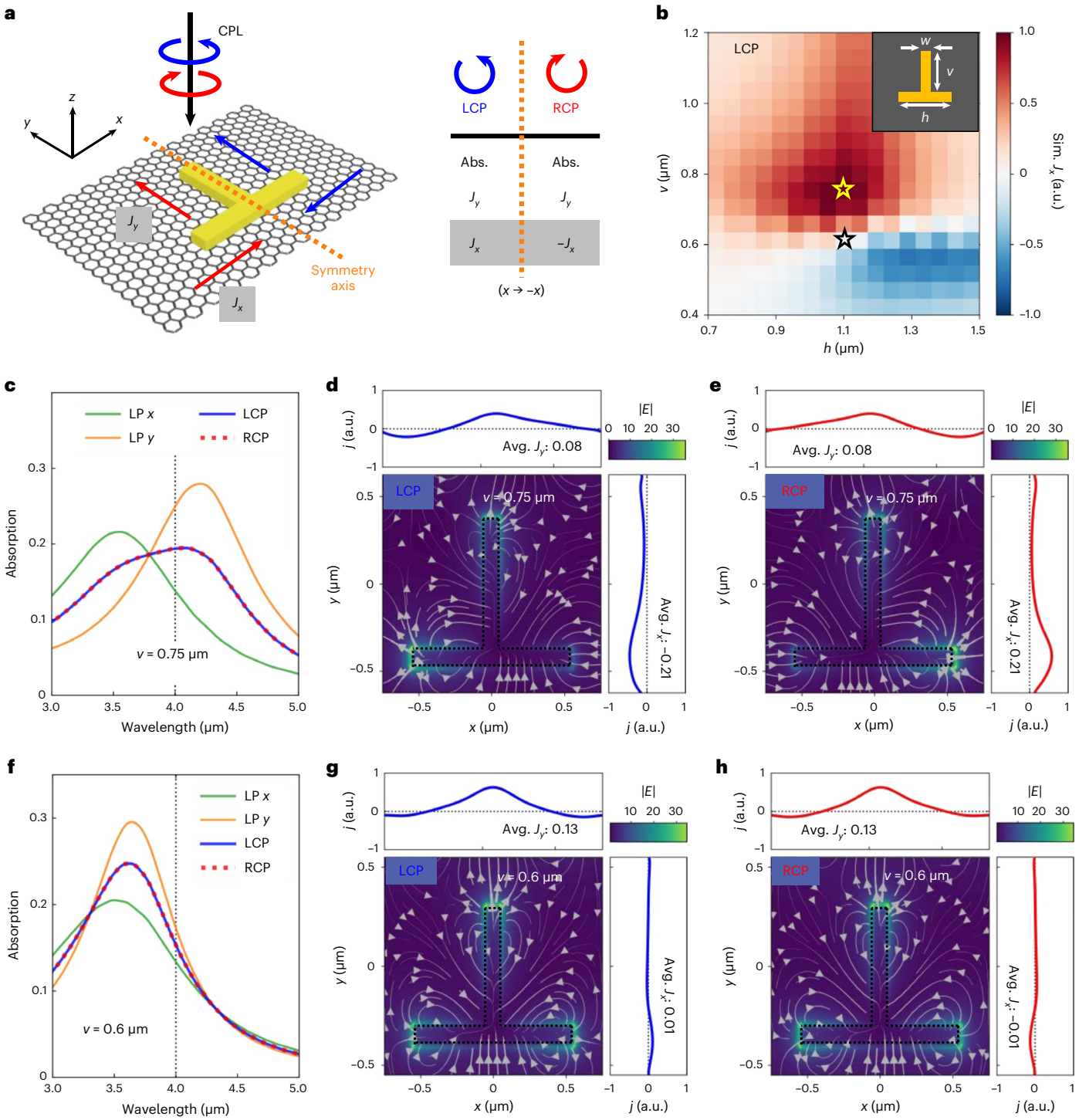

Fig. 2 | Mirror-symmetric meta-atoms with infinite discrimination ratio. **a**, Symmetry analysis of the photoresponse in our designed achiral plasmonic nanostructure, which sits on a graphene sheet. J_x and J_y denote the vectorial photocurrents along the x and y directions, respectively. LCP, left-handed CPL; RCP, right-handed CPL. Note that the handedness of CPL in this work is defined from the point of view of the source. Under the reflection operation ($x \rightarrow -x$), the absorption of the nanostructure and J_y are parity-even and hence respond identically to LCP and RCP. In contrast, J_x is parity-odd and thus CPL-sensitive. **b**, Calculated J_x under RCP illumination in the parameter space of the nanostructure consisting of two vertical and horizontal bars. The yellow and black open stars denote the geometry with an optimal CPL response (h = 1.1 μm and v = 0.75 μm) and almost vanishing CPL response (h = 1.1 μm and v = 0.6 μm), respectively. **c**,**f**, Simulated absorption spectra of the optimized CPL-sensitive (**c**) and CPL-insensitive (**f**) plasmonic nanostructures under linearly and circularly polarized illumination. **d**,**e**,**g**,**h**, Simulated near-field profile and corresponding photocurrent flow in graphene of the optimized (**d**,**e**) and CPL-insensitive (**g**,**h**) plasmonic nanostructures under LCP (**d**,**g**) and RCP (**e**,**h**) illumination. Grey lines denote the current flow. When the handedness of CPL changes, the averaged J_y remains, whereas the averaged J_x flips its sign. The resultant photoresponse discrimination ratio, g_{ph}, will then be infinite, protected by its achiral geometry.

Stokes parameters as $(R_0, R_1, R_2, R_3) \approx (0, 0, -0.18, 0.21)$. The vanished R_0 means that J_x is immune to the polarization-insensitive term, as a natural result of the mirror-symmetric geometry of our design. However, the non-vanishing R_2 indicates that our design is still affected by linearly polarized light. Such a dependence on linearly polarized light ubiquitously exists in all materials and structures except isotropic substances

https://doi.org/10.1038/s41566-022-01115-7

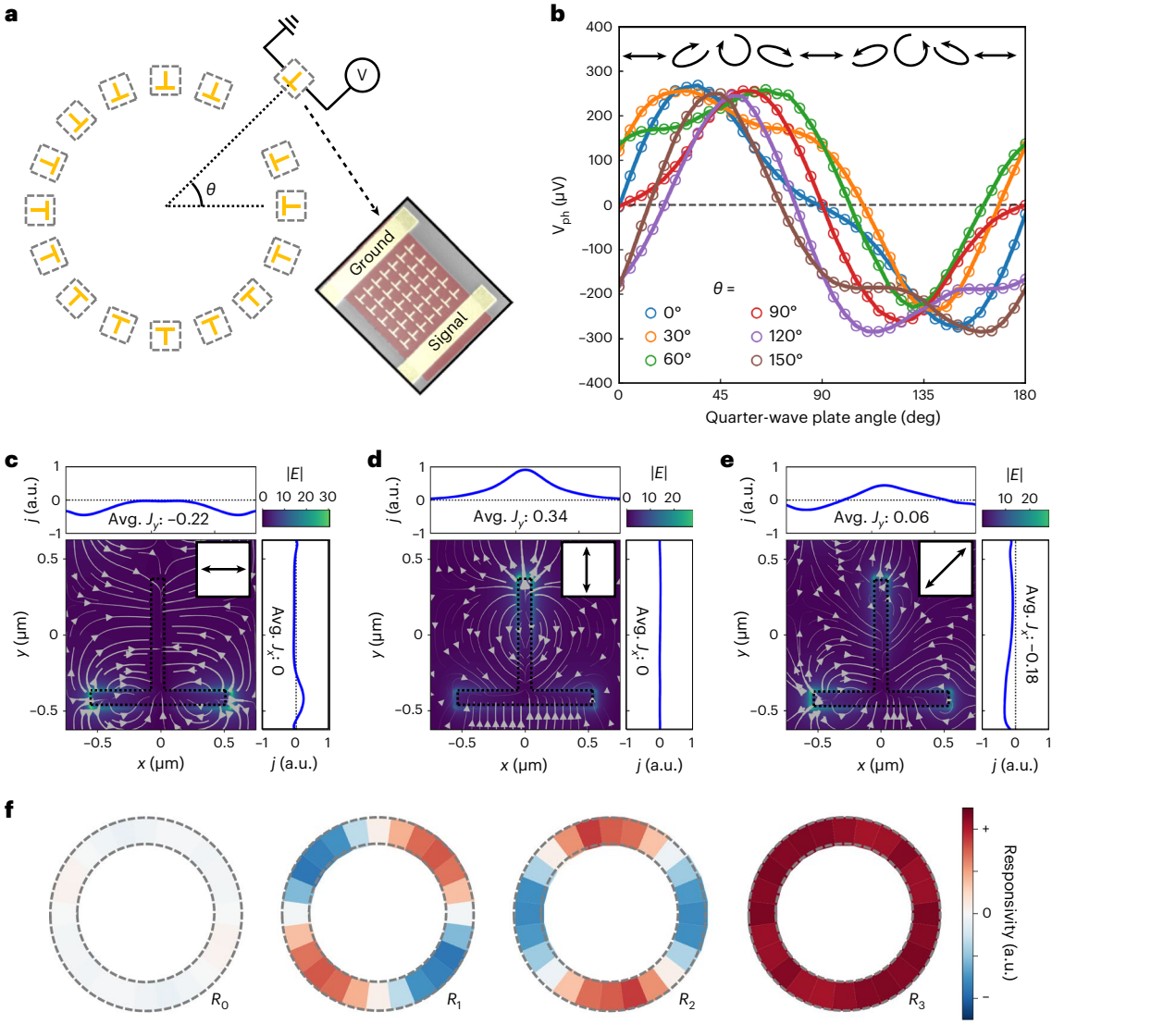

Fig. 3 | Rotational symmetry of the polarization-dependent responsivities in meta-atoms. a, Schematic of our approach to characterize the orientation-controlled polarization dependence of the plasmonic nanostructure. The nanostructure is rotated along with the electrodes at an angle of θ. Inset: the rectangular device used in our experiments. **b**, Measured polarization-dependent photovoltages at different θ. **c**–**e**, Simulated near-field profile and corresponding photocurrent flow of the optimized plasmonic nanostructure under 0° (**c**), 90° (**d**) and 45° (**e**) linearly polarized illumination. **f**, Extracted $R_{0,1,2,3}$ at different θ. Notably, R_0 vanishes everywhere due to the mirror symmetry of the meta-atoms. R_1 and R_2 follow the functions of $\sin(2\theta)$ and $-\cos(2\theta)$, respectively. R_3 is rotation-invariant. Therefore, the different rotational symmetries of $R_{0,1,2,3}$ of the meta-atoms allow us to achieve CPL-specific detection via geometrical arrangement.

with optical activity[42], which, unfortunately, in turn, forbids the vectorial photoresponse in a planar device (Supplementary Note 3).

To address the above bottleneck, we propose a geometric arrangement of nanostructures to realize a build-up in the CPL response and cancellation in the linearly polarized light, inspired by geometric metasurfaces where the nanostructures are rotated in a non-uniform manner to accumulate different geometric phases for the selective steering of polarization states[12,35]. The core of our method is the different polarization dependence of oriented nanostructures (as in the experimental schematic shown in Fig. 3a). In our experiments, we rotated a rectangular device by an angle of θ in steps of 15° and measured the photovoltages (Supplementary Fig. 13; Fig. 3b shows the results in steps of 30°, for clarity). Both the magnitude and sign of the photoresponse depend on the relative orientation of the nanostructures and the incident polarization states. Figure 3c–e shows the simulated photoresponse under illumination with different polarization angles. From the measured QWP-dependent photovoltages, we extract the θ-dependent Stokes responsivities, $R_{0,1,2,3}$ (Fig. 3f). As we have discussed, R_0 simply vanishes everywhere. Notably, R_1 (~$\sin(2\theta)$) and R_2 (~$-\cos(2\theta)$) vary cyclically, resembling a geometric phase-like behaviour. In contrast, R_3 is rotation-invariant. Accordingly, we conclude that specific CPL detection can be achieved by means of geometrically arranged nanostructures (additional experimental support is provided in Supplementary Fig. 14).

In this Article we demonstrate three combination types: (1) a ring-shaped cascaded device with $\theta \in (-80°, 260°)$, where $R_1 \propto \int_{\theta=-80°}^{260°} \sin(2\theta)\mathrm{d}\theta \approx 0$ and $R_2 \propto -\int_{\theta=-80°}^{260°} \cos(2\theta)\mathrm{d}\theta \approx 0$, as already shown in Fig. 1e; (2) a half-ring-shaped cascaded device with $\theta \in (0°, 180°)$, where $R_1 \propto \int_{\theta=0°}^{180°} \sin(2\theta)\mathrm{d}\theta = 0$ and $R_2 \propto -\int_{\theta=0°}^{180°} \cos(2\theta)\mathrm{d}\theta = 0$, shown in Supplementary Fig. 15; (3) a cascaded rectangular device with $\theta \in (0°, 90°)$, where $R_1 \propto \sum_{\theta=0°,90°} \sin(2\theta) = 0$ and $R_2 \propto -\sum_{\theta=0°,90°} \cos(2\theta) = 0$ (shown later).

https://doi.org/10.1038/s41566-022-01115-7

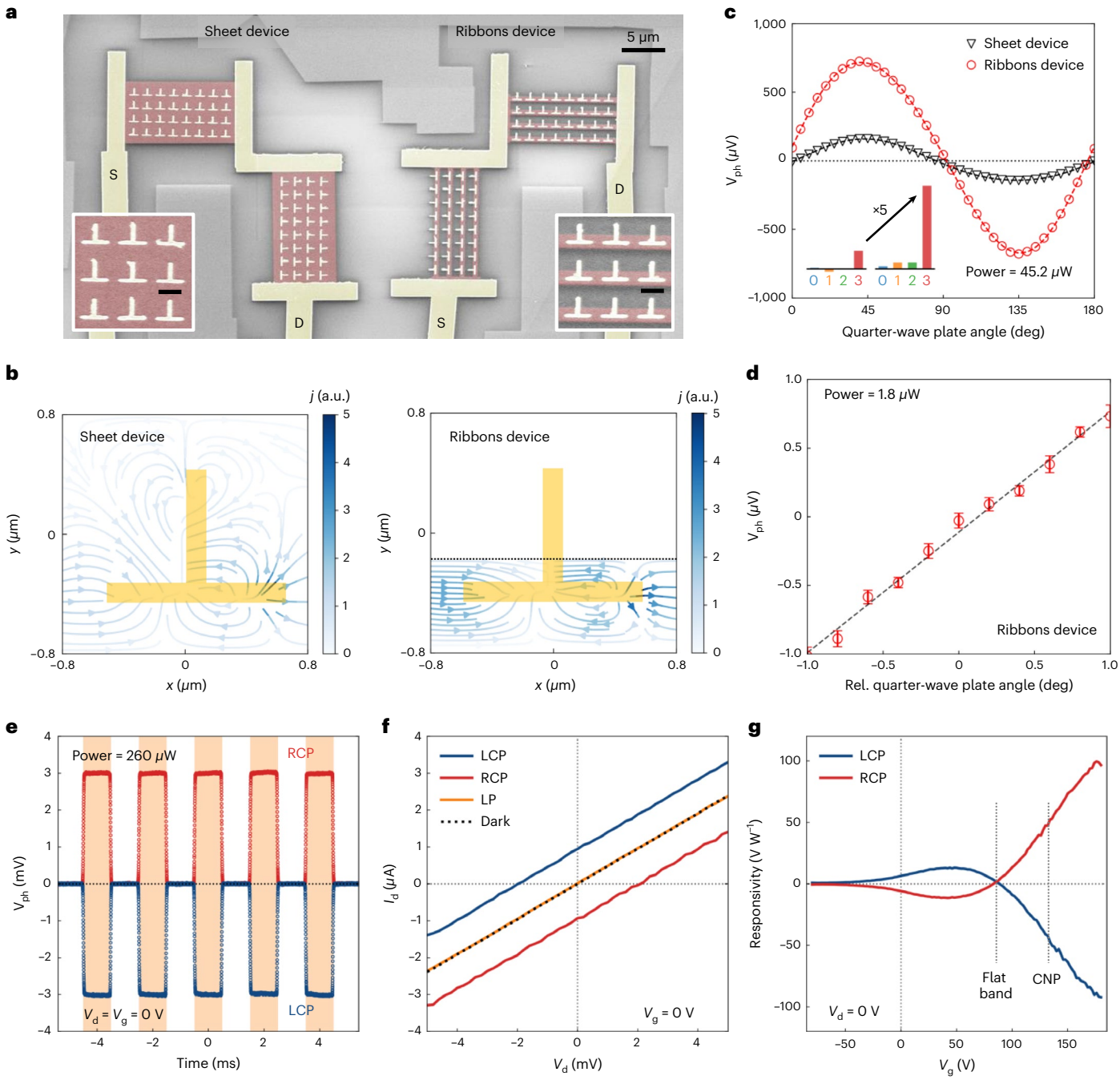

Fig. 4 | Enhanced CPL-specific detection using graphene ribbons. a, SEM images of the fabricated graphene sheet and ribbons devices. Scale bars (insets), 1 μm. **b**, Simulated current flow in the graphene sheet and ribbon devices. After removing the excess graphene, the ribbon device can guide the photocarriers better and possesses a larger internal resistance, thereby reducing the internal energy loss and increasing the external electrical output. **c**, Measured polarization-dependent photovoltages in the sheet and ribbon devices. Insets: the extracted responsivities, $R_{0,1,2,3}$, of the sheet device (left inset) and the ribbon device (right inset). Both devices specifically respond to the CPL, and the use of ribbons enhances the responsivity by five times, reaching 15 V W^{-1} at zero external bias. **d**, Fine measurement of the optical ellipticity at a small incident power of 1.8 μW, showing a detectivity of 0.03° Hz$^{-1/2}$. Error bars are the standard errors of the mean from 12 measurements. **e**, Measured photovoltages during on–off cycles of LCP and RCP light illumination. Orange shading indicates the light condition with an illumination power of 260 μW. **f**, Measured *I*–*V* curves with drain–source bias. The *x* and *y* axes intersections represent open-circuit voltages and short-circuit currents. LP, linearly polarized light. **g**, Measured gate-tunable photoresponse. No drain–source bias, V_d, was applied. CNP, charge neutral point of graphene. The peak responsivity of the four-column ribbon device reaches 98 V W^{-1}, corresponding to a responsivity of 392 V W^{-1} in single-column nanostructures.

From the viewpoint of practical application, the ring- and half-ring-shaped devices have relatively smaller fill factors of ~40%, meaning that 60% of the device area is blind to the incident light if detector arrays are considered (Supplementary Fig. 25). On the other hand, the fill factor of cascaded rectangular devices, in principle, could be close to 100%, so they are superior to curved device shapes.

Enhanced CPL-specific detection using graphene ribbons

We next turn to the third criterion—a high-responsivity CPL detector. Graphene has long been noted for its low photoresponse efficiency as a result of its semimetallic nature[43]. Intuitively, the ubiquitous graphene sheet could form a short circuit around the nanostructures, reducing the external output. Closer scrutiny reveals that our design

only requires a small area of graphene to convert the optical near-field to voltages and convey the electrical signals to the external circuit. Accordingly, we can play with the geometry of the graphene layer to increase the photoresponse. As shown in Fig. 4a, we fabricated and compared two L-shaped cascaded devices, which use graphene sheets and ribbons to extract the near-field chirality of the nanostructures, respectively. The ribbon width in our experiments was chosen to be 0.6 μm, as a compromise between fabrication requirements and alignment error. Our simulation shows that the CPL-sensitive photoresponse is not affected as long as the graphene ribbons cover the left and right ends of the T-shaped nanostructure (Fig. 4b). The measured photoresponse of the ribbon device was five times larger than that of the sheet device, although the two devices have the same device area (Fig. 4c). This enhancement demonstration was repeated in another two pairs of devices (Supplementary Fig. 16). At an incident power of 45 μW and zero external bias, the extracted responsivities of the ribbon device are $R_{0,1,2,3} \approx (0.03, 0.08, 0.08, 1) \times 15\ \mathrm{V\ W^{-1}}$, corresponding to a g_{ph} of 33. Considering that our device consists of four parallel-connected columns, which increase the photocurrent response but not the photovoltage response, the photovoltage responsivity of the individual nanostructures is 60 V W^{-1}.

Without applying any bias, our device has no dark current and hence a very low noise level, down to 10 nV Hz$^{-1/2}$ above 100 Hz, approaching its Johnson noise limit (Supplementary Fig. 17). The noise-equivalent power is as low as 0.67 nW Hz$^{-1/2}$. For a given incident power, P, the detectivity of optical ellipticity can be formulated as $D_{\mathrm{ellipticity}} = (180°/\pi) \times N_{\mathrm{light}}/(2R_3 \times P)$, where N_{light} is the power-dependent light noise. At a small incident power of 1.8 μW, our device can measure the ellipticity down to 0.03° Hz$^{-1/2}$ (Fig. 4d). See Methods and Supplementary Fig. 18 for details.

Figure 4e shows the measured photovoltages during 500-Hz on–off cycles under LCP and RCP light illumination. Supplementary Fig. 19 shows the almost constant response up to 4,000 Hz. We then used a pulsed laser to probe the rise and fall times at 886 ns and 902 ns, respectively, which are limited by the set-up (Supplementary Figs. 20 and 21). The measured photoresponse speed is much faster than most mid-infrared detectors such as thermopiles and microbolometers[44,45].

The linear I–V dependence in Fig. 4f indicates the ohmic contact in graphene devices. Under LCP and RCP illumination, the I–V lines shift upwards and downwards, illustrating their opposite photoresponse. By applying a gate voltage, the peak responsivity of the four-column device reaches 98 V W^{-1} at V_g = 180 V, corresponding to a responsivity of 392 V W^{-1} in the single-column nanostructures (Fig. 4g). A comparison with typical infrared detectors is provided in Supplementary Table 1. The photoresponse vanishes at V_g = 86 V, where the flat band condition is met. The charge neutral point is achieved at V_g = 136 V, and the hole mobility is 2,446 cm^2 V^{-1} s^{-1} (Supplementary Fig. 22).

We also characterized the power-dependent photoresponse, showing good linearity (Supplementary Fig. 23), and calculated the wavelength-dependent photoresponse with a full-width at half-maximum of ~1 μm (Supplementary Fig. 24).

Discussion

This work conceptualizes and demonstrates geometry-empowered monolithic CPL-specific photodetectors with near-infinite discrimination ratios, immunity to non-CPL field components and high responsivity, setting a benchmark for future integrated on-chip polarimeters. We show the importance of geometry in integrated photodetectors for achieving novel functionality and high responsivity. Although bipolar CPL-specific detection has been reported in relation to the photogalvanic effect[28], the ratchet effect[46] and thermopiles[22], their responsivities are at least four orders lower than in our work, and clear guidelines are lacking. In any case, our demonstrated gate tunability is a uniquely advantageous feature that is unavailable in conventional bulky materials. Because the near-field of resonant nanostructures could reveal more information on the various attributes of light than far-field scattering[47,48], our demonstrated efficient and specific readout of the near-field with an electrical signal will be helpful for new functional optoelectronic devices. For example, our principle can be readily extended to the specific detection of other Stokes parameters, $S_{0,1,2}$ (Supplementary Note 5), and the resultant full-Stokes detection is desirable, especially for imaging applications[1,6]. More exciting is that geometric photodetectors are suited to appropriately deal with structured light, such as vector beams and optical vortices, the intensity and phase profile of which are space-variant[49]. The absorption of our current design is relatively low (Supplementary Fig. 27), and higher responsivity is possible by using a metallic substrate with a dielectric spacer to reduce the reflection loss[16]. Thanks to recent advances in wafer-scale single-crystal growth of graphene[50], our work provides new opportunities for integrated, cost-effective, functional optoelectronic devices.

Online content

Any methods, additional references, Nature Portfolio reporting summaries, source data, extended data, supplementary information, acknowledgements, peer review information; details of author contributions and competing interests; and statements of data and code availability are available at https://doi.org/10.1038/s41566-022-01115-7.

References

1. Rubin, N. A. et al. Matrix Fourier optics enables a compact full-Stokes polarization camera. *Science* **365**, eaax1839 (2019).
2. Martínez, A. Polarimetry enabled by nanophotonics. *Science* **362**, 750–751 (2018).
3. Xiong, J. & Wu, S.-T. Planar liquid crystal polarization optics for augmented reality and virtual reality: from fundamentals to applications. *eLight* **1**, 3 (2021).
4. Lu, J. et al. Enhanced optical asymmetry in supramolecular chiroplasmonic assemblies with long-range order. *Science* **371**, 1368–1374 (2021).
5. Sherson, J. F. et al. Quantum teleportation between light and matter. *Nature* **443**, 557–560 (2006).
6. Tyo, J. S., Goldstein, D. L., Chenault, D. B. & Shaw, J. A. Review of passive imaging polarimetry for remote sensing applications. *Appl. Opt.* **45**, 5453–5469 (2006).
7. Greenfield, N. J. Using circular dichroism spectra to estimate protein secondary structure. *Nat. Protoc.* **1**, 2876–2890 (2006).
8. Gansel, J. K. et al. Gold helix photonic metamaterial as broadband circular polarizer. *Science* **325**, 1513–1515 (2009).
9. Zhao, Y., Belkin, M. A. & Alù, A. Twisted optical metamaterials for planarized ultrathin broadband circular polarizers. *Nat. Commun.* **3**, 870 (2012).
10. Li, Z. et al. Non-Hermitian electromagnetic metasurfaces at exceptional points. *Prog. Electromagn. Res.* **171**, 1–20 (2021).
11. Dorrah, A. H., Rubin, N. A., Zaidi, A., Tamagnone, M. & Capasso, F. Metasurface optics for on-demand polarization transformations along the optical path. *Nat. Photon.* **15**, 287–296 (2021).
12. Pors, A., Nielsen, M. G. & Bozhevolnyi, S. I. Plasmonic metagratings for simultaneous determination of Stokes parameters. *Optica* **2**, 716–723 (2015).
13. Bai, J. et al. Chip-integrated plasmonic flat optics for mid-infrared full-Stokes polarization detection. *Photon. Res.* **7**, 1051–1060 (2019).
14. Basiri, A. et al. Nature-inspired chiral metasurfaces for circular polarization detection and full-Stokes polarimetric measurements. *Light: Sci. Appl.* **8**, 78 (2019).
15. Ishii, A. & Miyasaka, T. Direct detection of circular polarized light in helical 1D perovskite-based photodiode. *Sci. Adv.* **6**, eabd3274 (2020).
16. Li, W. et al. Circularly polarized light detection with hot electrons in chiral plasmonic metamaterials. *Nat. Commun.* **6**, 8379 (2015).

17. Chen, C. et al. Circularly polarized light detection using chiral hybrid perovskite. *Nat. Commun.* **10**, 1927 (2019).
18. Yang, Y., Da Costa, R. C., Fuchter, M. J. & Campbell, A. J. Circularly polarized light detection by a chiral organic semiconductor transistor. *Nat. Photon.* **7**, 634–638 (2013).
19. Zhang, L. et al. π-Extended perylene diimide double-heterohelicenes as ambipolar organic semiconductors for broadband circularly polarized light detection. *Nat. Commun.* **12**, 142 (2021).
20. Afshinmanesh, F., White, J. S., Cai, W. & Brongersma, M. L. Measurement of the polarization state of light using an integrated plasmonic polarimeter. *Nanophotonics* **1**, 125–129 (2012).
21. Li, L. et al. Monolithic full-Stokes near-infrared polarimetry with chiral plasmonic metasurface integrated graphene-silicon photodetector. *ACS Nano* **14**, 16634–16642 (2020).
22. Lu, F., Lee, J., Jiang, A., Jung, S. & Belkin, M. A. Thermopile detector of light ellipticity. *Nat. Commun.* **7**, 12994 (2016).
23. Dhara, S., Mele, E. J. & Agarwal, R. Voltage-tunable circular photogalvanic effect in silicon nanowires. *Science* **349**, 726–729 (2015).
24. Sun, X. et al. Topological insulator metamaterial with giant circular photogalvanic effect. *Sci. Adv.* **7**, eabe5748 (2021).
25. Hatano, T., Ishihara, T., Tikhodeev, S. G. & Gippius, N. A. Transverse photovoltage induced by circularly polarized light. *Phys. Rev. Lett.* **103**, 103906 (2009).
26. Shalygin, V. A., Moldavskaya, M. D., Danilov, S. N., Farbshtein, I. I. & Golub, L. E. Circular photon drag effect in bulk tellurium. *Phys. Rev. B* **93**, 045207 (2016).
27. Ganichev, S. D. et al. Spin-galvanic effect. *Nature* **417**, 153–156 (2002).
28. Ganichev, S. D. et al. Subnanosecond ellipticity detector for laser radiation. *Appl. Phys. Lett.* **91**, 091101 (2007).
29. Hentschel, M., Schäferling, M., Duan, X., Giessen, H. & Liu, N. Chiral plasmonics. *Sci. Adv.* **3**, e1602735 (2017).
30. Chen, Y. et al. Multidimensional nanoscopic chiroptics. *Nat. Rev. Phys.* **4**, 113–124 (2022).
31. Movsesyan, A., Besteiro, L. V., Kong, X., Wang, Z. & Govorov, A. O. Engineering strongly chiral plasmonic lattices with achiral unit cells for sensing and photodetection. *Adv. Opt. Mater.* **10**, 2101943 (2022).
32. Zu, S. et al. Deep-subwavelength resolving and manipulating of hidden chirality in achiral nanostructures. *ACS Nano* **12**, 3908–3916 (2018).
33. Horrer, A. et al. Local optical chirality induced by near-field mode interference in achiral plasmonic metamolecules. *Nano Lett.* **20**, 509–516 (2020).
34. Chen, Y., Gao, J. & Yang, X. Direction-controlled bifunctional metasurface polarizers. *Laser Photon. Rev.* **12**, 1800198 (2018).
35. Chen, Y., Yang, X. & Gao, J. Spin-controlled wavefront shaping with plasmonic chiral geometric metasurfaces. *Light Sci. Appl.* **7**, 84 (2018).
36. Wei, J. et al. Zero-bias mid-infrared graphene photodetectors with bulk photoresponse and calibration-free polarization detection. *Nat. Commun.* **11**, 6404 (2020).
37. Wei, J., Xu, C., Dong, B., Qiu, C.-W. & Lee, C. Mid-infrared semimetal polarization detectors with configurable polarity transition. *Nat. Photon.* **15**, 614–621 (2021).
38. Giovannetti, G. et al. Doping graphene with metal contacts. *Phys. Rev. Lett.* **101**, 026803 (2008).
39. Zuev, Y. M., Chang, W. & Kim, P. Thermoelectric and magnetothermoelectric transport measurements of graphene. *Phys. Rev. Lett.* **102**, 096807 (2009).
40. Song, J. C. W. & Levitov, L. S. Shockley–Ramo theorem and long-range photocurrent response in gapless materials. *Phys. Rev. B* **90**, 075415 (2014).
41. Gabor, N. M. et al. Hot carrier-assisted intrinsic photoresponse in graphene. *Science* **334**, 648–652 (2011).
42. Sturman, B. I. & Fridkin, V. M. in *Photovoltaic and Photo-refractive Effects in Noncentrosymmetric Materials*, 8 (CRC Press, 1992).
43. Liu, J., Xia, F., Xiao, D., García de Abajo, F. J. & Sun, D. Semimetals for high-performance photodetection. *Nat. Mater.* **19**, 830–837 (2020).
44. Hsu, A. L. et al. Graphene-based thermopile for thermal imaging applications. *Nano Lett.* **15**, 7211–7216 (2015).
45. Zeng, L. et al. Van der Waals epitaxial growth of mosaic-like 2D platinum ditelluride layers for room-temperature mid-infrared photodetection up to 10.6 μm. *Adv. Mater.* **32**, 2004412 (2020).
46. Olbrich, P. et al. Ratchet effects induced by terahertz radiation in heterostructures with a lateral periodic potential. *Phys. Rev. Lett.* **103**, 090603 (2009).
47. Yi, S. et al. Subwavelength angle-sensing photodetectors inspired by directional hearing in small animals. *Nat. Nanotechnol.* **13**, 1143–1147 (2018).
48. Kim, S. J. et al. Anti-Hermitian photodetector facilitating efficient subwavelength photon sorting. *Nat. Commun.* **9**, 316 (2018).
49. Forbes, A., de Oliveira, M. & Dennis, M. R. Structured light. *Nat. Photon.* **15**, 253–262 (2021).
50. Wang, M. et al. Single-crystal, large-area, fold-free monolayer graphene. *Nature* **596**, 519–524 (2021).

Methods

Simulation

The near-field profile and absorption of our designed nanostructures were simulated with the finite-difference time-domain method (FDTD Solutions package from Lumerical). The end-to-end distance between neighbouring nanostructures was set as 0.4 μm along both the x and y axes. The boundaries above and below the array of nanoantennas were perfectly matched layers ($N = 24$). The modelling of near-field-driven photocurrents in graphene was implemented by our Python codes, which solve the Navier–Stokes equations.

Device fabrication

We started the fabrication with a thermally oxidized (~285 nm) highly resistive Si wafer (10 kΩ cm, Nova Electronic Materials). Few-layer graphene flakes were mechanically exfoliated onto the wafer from natural graphite (NGS Naturgraphit) and identified with an optical microscope. Metallic alignment markers were fabricated with electron-beam lithography (EBL; JBX-6300FS, Jeol), electron-beam evaporation of 3/20-nm Ti/Au (AJA International) and liftoff in hot acetone at 65 °C for 1 h. Our EBL process comprised spin-coating of poly(methyl methacrylate) (PMMA) 495k A5 at 4,000 r.p.m., baking at 180 °C for 2 min, with an exposure dose of 1,300 μC cm^{-2}; development in methyl isobutyl ketone:isopropyl alcohol (MIBK:IPA) = 1:3 for 30 s and a rinse in IPA for 30 s; drying with a nitrogen gun. We then patterned the graphene sheet to the desired shapes (ring, half ring, L-shaped cascaded devices and ribbons) using a second EBL step and oxygen plasma etching (20-s.c.c.m. O_2, 20 W, 20 s, VITA, Femto Science). The samples were then annealed at 300 °C for 6 h in an Ar/H_2 atmosphere to remove the resist residues. Afterwards, plasmonic nanostructures and contact electrodes were patterned onto the graphene flakes by a third EBL step with an alignment accuracy of ~100 nm, followed by thermal deposition (5/60-nm Pd/Au, Kurt J. Lesker Company) and liftoff in hot acetone at 65 °C for 1 h. A fourth EBL stage and thermal deposition (5/80-nm Cr/Au) were used to fabricate the large electrodes for probing and wire bonding. Finally, we deposited a thin 12-nm-thick Al_2O_3 layer to encapsulate the device. This consisted of two steps. The first was the deposition of 2-nm metal Al with a high-vacuum electron-beam evaporator; this layer was quickly oxidized to form a uniform Al_2O_3 film on the graphene. The second step was the deposition of 10-nm Al_2O_3 by atomic-layer deposition. The Al_2O_3 layer helped reduce the doping level of the graphene device and hence increased the responsivity. The existence of the thin Al_2O_3 layer did not affect our probing (5-μm radius tip) and wire bonding. The L-shaped graphene sheet device and ribbons device were fabricated from the same graphene flake and in the same fabrication process to guarantee a fair comparison.

Characterization

We used a quantum cascade laser at a wavelength of 4 μm (MIRCat-1200, Daylight Solutions, polarization ratio > 100:1) as our light source. A low-order QWP (WPLQ05M-4000, Thorlabs) designed at 4 μm was used to control the polarization states of the light. The light was delivered onto the device by plane mirrors and an off-axis parabolic mirror (focal length = 101.6 mm, MPD149-P01, Thorlabs). Normal incidence was ascertained before the experiments. The open-circuit voltages were measured as the photoresponse with a lock-in amplifier (Stanford Research Systems, SR830), and the light signal was modulated by an optical chopper (Stanford Research Systems, SR540, up to 4-kHz modulation frequency) at ~280 Hz to get rid of the low-frequency noises and increase the signal-to-noise ratio. We used a filter slope of 24 dB oct^{-1}, and the resulting equivalent noise bandwidth (ENBW) of the lock-in amplifier was then $5/(64t)$, where t is the time constant. We used a time constant of 30 ms for noise measurements, corresponding to an ENBW of 2.6 Hz. The d.c. I–V curves and gate voltage dependence were measured with a semiconductor characterization system (Keithley 4200-SCS) without preamplifiers. The characterization of on–off cycles and response time were conducted by directly connecting the device to an oscilloscope (InfiniiVision DSOX3034T, Keysight, 350 MHz, 5 GSa s^{-1}). The average mode was used to increase the signal-to-noise ratio. The 1,000-ns pulse was generated by our QCL laser in pulse mode. The power level of the incident light was tuned with a set of neutral density filters and calibrated with a power meter (843-R, Newport).

Data availability

All data needed to evaluate the conclusions in this paper are present in the paper or the Supplementary Information. Additional data related to this paper may be requested from the corresponding authors upon request.

Acknowledgements

The authors acknowledge the financial support from the National Research Foundation (grant no. NRF-CRP22-2019-0006) and Advanced Research and Technology Innovation Centre (grant no. A-0005947-16-00). C.W.Q acknowledges the financial support from the National Research Foundation (grant no. NRF-CRP26-2021-0004). C.L. acknowledges financial support from the National Research Foundation Singapore (grant no. NRF-CRP15-2015-02). Y.C. acknowledges support from start-up funding of the University of Science and Technology of China and the CAS Pioneer Hundred Talents Program. Y.L. acknowledges support from the National Natural Science Foundation of China (grant no. 92163123). W.L. acknowledges financial support from the National Natural Science Foundation of China (grants nos. 62134009 and 62121005) and the Innovation Grant of Changchun Institute of Optics, Fine Mechanics and Physics (CIOMP). K.S.N. is grateful to the Ministry of Education, Singapore (Research Centre of Excellence award to the Institute for Functional Intelligent Materials, I-FIM, project no. EDUNC-33-18-279-V12) and Royal Society (UK, grant no. RSRP\R\190000) for support.

Author contributions

J.W. and C.-W.Q. conceived the project. J.W. and Y.C. carried out the theoretical analysis and numerical simulations. J.W. fabricated the samples. J.W., J.X. and C.L. carried out and contributed to the device characterization. J.W., Y.C., Y.L., W.L., C.L., K.S.N. and C.-W.Q. discussed and analysed the numerical and experimental results. All authors discussed and contributed to the manuscript. C.-W.Q. oversaw the whole project.

Competing interests

The authors declare no competing interests.

Additional information

Supplementary information The online version contains supplementary material available at https://doi.org/10.1038/s41566-022-01115-7.

Correspondence and requests for materials should be addressed to Chengkuo Lee or Cheng-Wei Qiu.

Peer review information *Nature Photonics* thanks the anonymous reviewers for their contribution to the peer review of this work.